Defect-Limited Mobility and Defect Thermochemistry in Mixed A-Cation Tin Perovskites: (CH3NH3)1–xCsxSnBr3

Defect-Limited Mobility and Defect Thermochemistry in Mixed A-cation Tin Perovskites: $(CH_3NH_3)_{1-x}Cs_xSnBr_3$

Dominic C. Asebiah,[†,△] Eve M. Mozur,[‡,¶,△] Alexandra A. Koegel,[‡] Adair Nicolson,[§,‖] Seán R. Kavanagh,[⊥] David O. Scanlon,[‖] Obadiah G. Reid,[*,#,@] and James R. Neilson[*,‡,†]

†*School of Materials Science & Engineering, Colorado State University, Fort Collins, CO 80523, United States*

‡*Department of Chemistry, Colorado State University, Fort Collins, CO 80523, United States*

¶*Department of Materials Science & Metallurgy, Colorado School of Mines, Golden, CO*

§*Department of Chemistry, University College London, 20 Gordon Street, London WC1H 0AJ, U.K.*

‖*School of Chemistry, University of Birmingham, Edgbaston, Birmingham B15 2TT, U.K.*

⊥*Harvard University Center for the Environment, Cambridge, MA 02138, United States*

#*Renewable and Sustainable Energy Institute, University of Colorado Boulder, Boulder, CO 80303, United States*

@*Chemistry & Nanoscience Center, National Renewable Energy Laboratory, Golden, CO 80401, United States*

△*Contributed equally to this work*

E-mail: obadiah.reid@nrel.gov; james.neilson@colostate.edu

Abstract

Hybrid organic-inorganic semiconductors crystallizing in the perovskite structure present a significant opportunity for realizing defect-tolerant semiconductors. In this

work, we examine the solid solution, $(CH_3NH_3)_{1-x}Cs_xSnBr_3$, and identify the thermochemistry dictating the intrinsic carrier concentrations and how local structural distortions influences this electronic behavior. This family of compounds exhibits the expected systematic trend in decreasing optical gap with the cesium to methylammonium A-site mixing ratio, x, in the visible region. However, the carrier mobility, as determined from time-resolved microwave conductivity measurements, trends opposite to that expected from first-principles calculations combined with Boltzmann scattering theory calculations of the carrier mobility. We propose that this is a result of increasing carrier scattering with x in $(CH_3NH_3)_{1-x}Cs_xSnBr_3$ due to a significant increase in the carrier density with x. By examining the dependence of the carrier density as a function of x, we infer the compositional-dependence of the average enthalpy and non-configurational entropy per defect. While diffraction reveals a cubic aristotypic perovskite structure as a function of x at room temperature, the pair distribution functions obtained from synchrotron X-ray total scattering from these materials are better described by symmetry-adapted displacement modes of the $Pm\bar{3}m$ crystal structure, which we attribute to a large degree of anharmonic dynamics of the atom positions. This analysis shows that $CH_3NH_3^+$-rich compositions retain mostly linear Sn–Br–Sn bonding environments through the displacements, while Cs^+-rich compositions lead to more significantly bent Sn–Br–Sn environments. We propose that these bent bonding arrangements in Cs-rich compositions yield a higher propensity for defect formation. This also provides a rationale for carrier trapping that gives rise to anomalous microwave transients. Together, these results provide insight into the structure-dynamics-properties relationships in this highly anharmonic system with high amplitude atomic motions and low defect formation energies.

Keywords

hybrid perovskites; pair distribution function analysis; defect thermochemistry; microwave conductivity

1 Introduction

Hybrid halide perovskites have emerged as promising materials for optoelectronic applications owing to their ease of solution processing, defect tolerance, and long charge carrier lifetimes.[1,2] Hybrid halide perovskites typically exhibit a general formula, ABX_3, where A = Cs^+, $CH_3NH_3^+$ (MA), or $CH(NH_2)_2^+$ (FA), B = Sn, Ge, or Pb, and X = Cl, Br, or I. The corner-linked octahedra found in the cubic crystal structure ($Pm\bar{3}m$ symmetry) provide nominally ideal orbital overlap between the B and X species, upon which the frontier electronic states exist.

While lead-based materials have shown the most promising initial properties and performance in photovoltaic devices, the lower band gap and reduced toxicity of tin-based materials motivate fundamental research into their materials' chemistry. Sn-based perovskites exhibit two primary aspects that merit further study:[3–5] (1) adventitious oxidation of Sn^{2+} to Sn^{4+} leads to high hole concentrations with significantly reduced carrier mobilities;[6–9] (2) a higher propensity to form stereochemically-active lone pairs (relative to Pb) can drive metal off-centering thus renormalizing the electronic structure and decreasing mobilities.[10–12] Such metal off-centering and anharmonic effects can yield significant changes to the physical properties.[13] As such, fundamental studies elucidating how the chemistry influences these qualities are needed.

Methylammonium and cesium tin bromide both exhibit significant visible light absorption and crystallize in the cubic perovskite crystal structure at ambient temperature. The optical bandgap of $CH_3NH_3SnBr_3$ is reported to range between 2.1 and 2.3 eV,[14–16] and that of $CsSnBr_3$ is reported to range between 1.75-1.80 eV,[17–22] suggesting potential applications as a top absorber layer on Si in tandem photovoltaic devices.[23] The reported electron mobility in $CH_3NH_3SnBr_3$ is sparse and inconsistent, varying from 10^{-5} cm^2V^{-1} s^{-1} in field-effect measurements on thin films[24] to 320 cm^2 V^{-1} s^{-1} in Hall-effect measurements on single crystals,[25] thus suggesting a very strong sensitivity to defects and processing conditions. The experimentally-determined mobility for $CsSnBr_3$ is also not widely available.

One study found 2-20 $cm^2\ V^{-1}\ s^{-1}$ via Hall effect measurements on non-annealed thin films and 140-1000 $cm^2\ V^{-1}\ s^{-1}$ after annealing.[26] The theoretical mobility spans from 260 to 511 $cm^2V^{-1}s^{-1}$.[27,28] In summary, these materials have promising fundamental properties but with myriad unresolved questions.

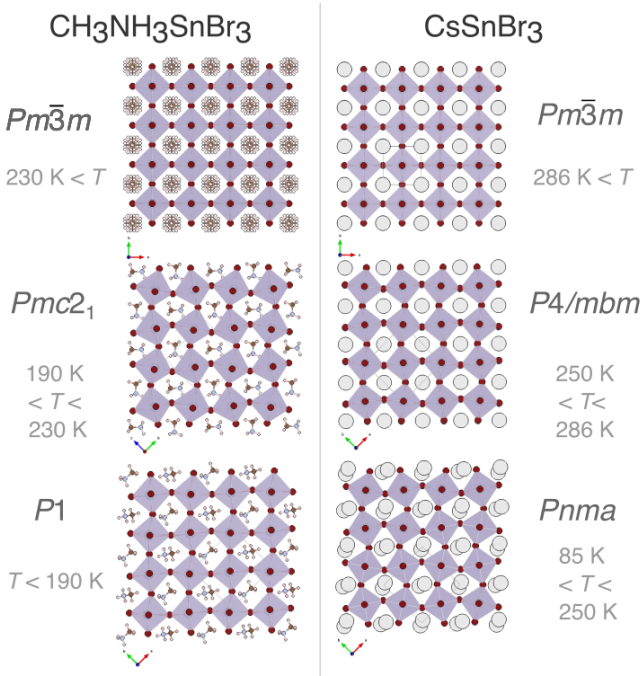

Figure 1: Schematic illustration of the crystal structures of $CH_3NH_3SnBr_3$ and $CsSnBr_3$ as a function of temperature. While $CsSnBr_3$ undergoes simple tilting displacements similar to many other perovskites above $T = 85$ K, $CH_3NH_3SnBr_3$ exhibits a polar distortion resulting in the $Pmc2_1$ space group on cooling, followed by a yet-unknown triclinic structure, illustrated by a DFT-minimized result[29] described in $P1$ symmetry.

Within the cubic phase, high-amplitude cation-off centering distortions arising from stereochemically active lone pairs persist dynamically in both materials, as revealed by a combination of density functional theory calculations and pair distribution function analysis.[10,12,30] However, $CH_3NH_3SnBr_3$ and $CsSnBr_3$ exhibit different phase transitions upon cooling (Figure 1), suggesting that the nature of these local distortions is different. Specifically, $CH_3NH_3SnBr_3$ undergoes a transition to an orthorhombic phase (space group: $Pmc2_1$, T = 230 K), followed by a transition to an unknown triclinic phase (T= 190 K) with the atomistic structure estimated from DFT-based relaxation,[29] as illustrated in Fig-

ure 1. In this structure, the [$SnBr_6$] octahedra are acentric and co-aligned to yield the polar space group. In contrast, upon cooling, $CsSnBr_3$ undergoes a transition to a tetragonal phase with in-phase octahedral tilting (space group: $P4/mbm$; Glazer tilt; $a^0a^0c^+$), followed by an orthorhombic phase (space group: $Pnma$, Glazer tilt $a^+b^-b^-$), as found in many other perovskites (e.g.$CsSnI_3$,[31,32] $CsPbCl_3$,[33] $CsPbBr_3$[34]). Even more curious, $CsSnBr_3$ exhibits further phase transitions below 100 K: "Phase II" (77 K $< T <$ 85 K, space group $P2_1/m$) exhibits noncollinear acentric Sn(II) displacements to result in ferroaxial order; "Phase I" ($T <$77 K, space group $P2_1$) exhibits a spontaneous polarization and chirality due to alignment of the Sn(II)-derived lone pairs.[35] As such, it is perhaps less surprising that the pair distribution functions exhibit strong deviations from the cubic structure at room temperature due to the nature of the high-amplitude and anharmonic atomic displacements that condense into complex orders at low temperatures.

In this contribution, we report how the A-site cation influences the local distortions and in turn, optoelectronic properties by way of carrier localization in $(CH_3NH_3)_{1-x}Cs_xSnBr_3$. The crystal structures reflect solid solution behavior between $CH_3NH_3SnBr_3$ and $CsSnBr_3$, with a miscibility gap and two-phase coexistence for $0.45 < x < 0.75$. UV-Visible spectroscopy reflects a decrease in the optical gap with increasing x. Time-Resolved Microwave Conductivity (TRMC) reveals an exponential decrease in the carrier mobility with x, which counters the predictions from Boltzmann scattering theory calculations with inputs generated by density functional theory. From the composition dependence of the carrier concentration, we estimate the enthalpy and non-configurational entropy associated with defect generation. Symmetry-adapted displacement mode analysis of pair distribution functions (PDF) obtained from synchrotron X-ray total scattering data collected between 100 K and 420 K reveals that all samples exhibit local distortions of the average cubic symmetry, consistent with dynamic stereochemical activation of lone pairs. Modelling the PDFs, we see a systematic trend with x in that MA-rich samples tend to preserve some linear Sn–Br–Sn bond geometries (Γ_4^- Br A_{2u} mode), whereas Cs-rich samples have a preference for bent

Sn-Br-Sn coordination (Γ_4^- Br E_u mode). This preference for a bent Sn–Br–Sn coordination may assist in carrier trapping that yields to anomalous signals in the TRMC experiments. Compositional tuning reveals the relationship between variable carrier localization and the local distortions in $(CH_3NH_3)_{1-x}Cs_xSnBr_3$.

2 Methods

2.1 Sample preparation

All the sample preparation steps were carried out in an argon atmosphere. A 3 g sample of $CH_3NH_3SnBr_3$ was synthesized from CH_3NH_3Br and $SnBr_2$ in an anhydrous ethanol solution, as previously described.[36] Briefly, CH_3NH_3Br (0.86 g) was dissolved in 20 ml of anhydrous ethanol solution, and this solution was slowly added, drop-by-drop, into 30 ml of an anhydrous ethanol solution of $SnBr_2$ (2.14 g) while boiling and stirring. A deep red solid precipitates upon slow cooling of the solution to 25 °C. The solution was decanted, and the precipitate dried. Cesium tin bromide ($CsSnBr_3$), 3 g, was prepared from the halide binaries CsBr (1.30 g) and $SnBr_2$ (1.70 g). Stoichiometric amounts of cesium bromide and tin(II) bromide were ground together, pelleted, and sealed in a quartz ampoule under vacuum. Samples were then heated to 400 °C over 6 h, held at that temperature for 6 h, and then the furnace was cooled to room temperature, 25 °C per minute. The solid solution series of $(CH_3NH_3)_{1-x}Cs_xSnBr_3$ were prepared by grinding the stoichiometric quantities of the end member perovskites. The powders were pelleted, sealed in a quartz ampoule, and placed in a convection oven at 150 °C for 5 to 7 days. Compositions were synthesized targeting x values of 0, 0.04, 0.1, 0.2, 0.3, 0.4, 0.5, 0.6, 0.7, 0.8, 0.96, and 1, with an observed miscibility gap between $0.45 < x < 0.75$.

Non-electrically-continuous thin film samples of dispersed powders for microwave conductivity experiments were prepared using a polystyrene binder. All procedures were conducted within an argon-filled glovebox. The compositions of x in $(CH_3NH_3)_{1-x}Cs_xSnBr_3$

powders ($\approx$ 200 mg) were mixed with polystyrene ($\approx$ 200 mg) in benzene ($\approx$ 2 ml). The solution was stirred until the polystyrene dissolved. Each solution, with an average concentration of $\approx$ 14.5 mole formula unit per liter or $\approx$ 3 wt%, was drop-cast onto 25$\times$11$\times$1 mm UV-fused silica substrates and annealed at 60 °C on a hot plate for 10 min to evaporate the benzene. The presence of polystyrene aids in adhering the various compositions of x in $(CH_3NH_3)_{1-x}Cs_xSnBr_3$ onto the 25$\times$11$\times$1 mm UV-fused silica substrates upon the benzene evaporation. The prepared samples were stored in vials under argon atmosphere and sealed in vacuum storage bags to prevent air exposure before being transported for TRMC measurements.

2.2 Diffraction data collection

Laboratory powder X-ray diffraction (PXRD) data were acquired using a Cu Kα radiation source and a Lynxeye XE-T position-sensitive detector on a Bruker D8 Discover X-ray diffractometer to check phase purity. Samples were mounted on a "zero diffraction" Si wafer and covered in polyimide tape prior to measurement. Crystallite sizes were estimated from analysis of the peak broadening in the PXRD data. As the Bragg reflections were broadened beyond the instrument resolution, the Lorentzian linewidth was used to extract the crystalline coherence length as a function of x in $(CH_3NH_3)_{1-x}Cs_xSnBr_3$ using the Rietveld method implemented in TOPAS v6.

Temperature-dependent synchrotron powder X-ray diffraction (SXRD) patterns were obtained on the diffractometer 28-ID-1 at the National Synchrotron Light Source II, Brookhaven National Laboratory (λ = 0.1668 Å) between T = 420 K and T = 100 K at ΔT = 20 K intervals. Samples were held in evacuated and flame-sealed extruded fused silica capillaries with an outer diameter (OD) of 1.1 mm and inner diameter (ID) of 0.9 mm. The detector employed in the diffractometer 28-ID-1 at NSLS-II Beamline is the PILATUS3 X 2M CdTe Detector, positioned 1204.49 mm from the sample. $BaTiO_3$ and Ni were used as calibration standards.

2.3 Total scattering data collection

Total scattering data were collected at beamline 11-ID-B at the Advanced Photon Source, Argonne National Laboratory (λ = 0.1423 Å) between T = 420 K and T = 100 K in ΔT = 10 K intervals. Powders were epoxy-sealed in extruded fused silica capillaries with an outer diameter (OD) of 1.1 mm and an inner diameter (ID) of 0.9 mm under a nitrogen environment. The Perkin Elmer XRD1621 amorphous silicon detector, positioned 250 mm from the sample, was utilized in this experiment. Each scan, per sample, and temperature had an exposure time of 0.5 seconds, resulting in a cumulative exposure time of 3 min for data collection from each sample. A total of 360 frames constituted each scan. CeO_2 (SRM674b) was utilized as the calibrant for the experiment and calibration procedures were conducted to optimize distances and tilt angles, enhancing precision across all samples. PDFgetX3[37] was used to normalize the data into $S(Q)$ and transform the data into the pair distribution function, $G(r) = \frac{2}{\pi}\int_{Q_{min}}^{Q_{max}} Q[S(Q)-1]\sin(Qr)dQ$.

2.4 Pair distribution function analysis

Standard PDF structure refinements were carried out in PDFgui[38] while displacement mode refinements were carried out in TOPAS v6. From the measurement of polycrystalline Ni powder, we obtained the instrumental factors, $Q_{\text{max}} = 25$ Å^{-1}, Q_{broad} = 0.01701 Å^{-1}, and Q_{damp} = 0.03328 Å^{-1}, as defined by PDFgui,[38] and included their equivalent terms in subsequent modelling with TOPAS v6, as described below. The PDF was rebinned at Δr = 0.05 to minimize overfitting.

ISODISTORT[39] was used to generate symmetry-adapted distortion modes[40] by decomposing the cubic perovskite into the structure defined by Swainson et al. within space group $Pmc2_1$.[29] While $CH_3NH_3SnBr_3$ and $CsSnBr_3$ both exhibit lower symmetry phases at lower temperatures, the $Pmc2_1$-based structure provides an ideal compromise of permitting distortions but without too many degrees of freedom. For consistent referencing of the

structure between publications, we employ the a basis for the $Pmc2_1$ structure relative to the cubic structure by $((0,0,1),(1,\bar{1},0),(1,1,0))$; origin $= (-0.2678, -0.7678, 1/2)$), where the cubic structure is defined with Sn at $\vec{x} = (0,0,0)$; Br at $\vec{x} = (1/2,0,0)$, and Cs used to replace the rotationally-disordered methylammonium molecule at $\vec{x} = (1/2,1/2,1/2)$. In the refinements, Cs was replaced with a methylammonium defined by rigid-body constraints; the molecule's position and orientation were allowed to refine freely, while the occupancies of the methylammonium atoms and Cs atom were defined by the nominal sample composition (e.g., $(CH_3NH_3)_{1-x}Cs_xSnBr_3$). Given that the hybrid perovskites suffer from significant anharmonic dynamics,[10,30] this posed a significant challenge for the peak shape in the PDF,[41] particularly with respect to the r-dependent broadening due to the transition from correlated (low r) to uncorrelated (high r) motion.[42] A detailed description of this analysis is provided in the Supporting Information. Mode amplitudes were permitted to refine one at time across all compositions to inspect what provided the largest improvement in the goodness of fit across the series. Self-consistent examination of the modes (mode definitions provided in the representative TOPAS input file provided as Supporting Information) revealed that only 4 modes were needed to provide the best fit across all compositions (Γ_4^- Br A_{2u}, Γ_4^- Br E_u, M_3^+ Br E_u, Γ_4^- Cs T_{1u}). While incorporating additional modes could increase the goodness-of-fit by slight amounts, this set of four modes provided the minimal model that could provide the best fit across the series of compounds.

2.5 UV-Visible Spectroscopy

Diffuse reflectance optical spectroscopy measurements were conducted using an Ocean Optics tungsten-halogen light source (Mikropack HL-2000) and an Ocean Insight flame miniature spectrometer (Flame-S-VIS-NIR) with an integrating sphere. A fiber-optic cable was used to illuminate the flat base of a borosilicate glass vial filled with loose powder of the reaction products. A vial containing $BaSO_4$ was utilized as a white reflectance standard.

The vials containing the reaction products were sealed with electrical tape to maintain an inert atmosphere (argon-filled glovebox) before being removed for measurement. The Kubelka–Munk transform was calculated using the formula $(k/s) = ((1 - R_\infty)^2)/(2R_\infty)$, where k is the absorption coefficient, s is the scattering coefficient, and R_∞ is the diffuse reflectance (see Supporting Information for alternative analyses).

2.6 Scanning Electron Microscopy

Scanning electron microscopy (SEM) was conducted using a JEOL JSM-6500 instrument at Colorado State University operating at 5 keV, with the scanning beam positioned perpendicular to the sample surface. Samples were mounted on a gold-coated stub, and eight images were captured from different areas of each sample under consistent conditions, including a working distance of 10 mm, to facilitate comparison. An electron beam scanned the vacuum-contained sample surface in a raster pattern to produce realistic topography SEM images. Secondary electrons emitted from the impinged surface points were collected by a fixed in-column detector, with slight variations in the angle between the electron beam and the sample surface.

The captured SEM images were analyzed using ImageJ software.[43] The data generated from the ImageJ analyses of each sample's image were plotted in histograms, with the x-axis representing the diameter of the particle sizes of each image and the y-axis representing the pixel frequency. Histograms from all images were combined and averaged to reduce noise and account for minor nonuniformity in the sheet at the microscopic level. The uncertainty calculated from multiple triplicate measurements was less than 1%.

2.7 Time-Resolved Microwave Conductivity

The Time-Resolved Microwave Conductivity (TRMC) measurements were carried out following the methods described in previous studies.[44,45] Samples were loaded into the mi-

crowave cavity in a nitrogen glove box and purged continuously with nitrogen during the transient measurements. However, the thick films of perovskite powders bound in polystyrene that we employ in this study required new electromagnetic simulations of the cavity response to interpret.[44] These simulations enabled us to quantify the equilibrium (dark) conductivity, dielectric constant, and photoconductivity of these samples.

All the microwave measurements in this study are based on perturbation of the properties of a microwave resonator in which the sample is enclosed, either in response to introduction of the sample or photoexcitation. They provide the effective complex conductivity or (equivalently) the complex dielectric constant of the sample.[46] In the context of semiconductor samples, this is often most usefully expressed as a real conductivity and a real dielectric constant, but the real part of the conductivity may also contain contributions better thought of as dielectric loss (e.g., mobile dipoles or optical phonons). To a first approximation, the shift in resonance frequency (near 9 GHz) is related to the sample dielectric constant (or imaginary conductivity) and the shift in depth and width is identified with the real conductivity (or imaginary dielectric constant).

In practice, dark conductivity data are obtained by measuring the power reflection coefficient as a function of microwave frequency in the vicinity of the resonance (a "resonance curve") and comparing it with our simulations. We measure the empty cavity, the cavity with a blank slide inserted, and the cavity holding the sample. The empty cavity has its resonance shifted to high enough frequency that it is useful as a blank, giving the incident microwave power (as $\approx 100\%$ is reflected in this instance). The quartz slide provides a reference point in resonance frequency, curve depth, and width, to which the sample is compared via our electromagnetic simulations to extract its properties (as provided in the Supporting Information). Notably, these values must then be renormalized to account for the difference between sample volume in the electromagnetic simulations and that employed in the experiments. The latter is quantified using the measured mass and unit-cell density of each perovskite formulation we measure.

Photoconductivity measurements utilized an Nd:YAG laser system incorporating a 355 nm pumped optical parametric oscillator (OPO) for sample excitation (Spectra-Physics PremiScan ULD/500 OPO, pumped by a Spectra-Physics Quanta-Ray, or the Continuum Panther OPO pumped by a Continuum Powerlite). The transients of TRMC with fits for all samples are shown in Figure S7. Excitation for every sample was either at 532 nm (2.33 eV) or 550 nm (2.25 eV), with the end-members excited at 532 nm and the alloys at 550 nm. The slight difference in pump energy is an inconsequential experimental variation (0.076 eV) and both are well above the band gap of all the materials (2.1 eV / 590 nm).

Quantification of the photoconductivity measurements relies on the same electromagnetic simulations. The fits to the dark resonance data provide a point in the parameter space of cavity simulations, and the derivative of cavity characteristics with respect to sample properties provides sensitivity factors needed to quantify transient changes in both dielectric constant and conductivity.[46,47] In many cases the transient behavior of semiconductors appears as an almost entirely real conductivity response, in which case it is only necessary to monitor the change in resonance depth as a function of time. In the present case, however, there was a substantial frequency shift in the cavity observed upon photoexcitation for many of the samples, requiring measurements at three or more microwave frequencies in order to deconvolve the real and imaginary parts of the photoconductivity.[46,48–51] From appropriate calibration and simulation of the transient response,[44] the transient relays the product of the photon-to-carrier yield (ϕ) and sum of electron and hole mobilities ($\Sigma\mu$), expressed as the yield-mobility-product, $\phi\Sigma\mu$.

The transients were subsequently modeled using a multi-exponential function convolved with instrument response function. In this case we use an exponentially modified Gaussian with a 5 ns cavity response time and a 4 ns FWHM laser pulse. Results are calculated and presented as real and imaginary yield-mobility products, under the assumption that all incident light is absorbed by the thick rough films. A description of the fitting methods employed is provided elsewhere.[45]

The variabilities in thin film shape, substrate positioning, and cavity assembly reproducibility are the primary sources of measurement errors in dark conductivity and dielectric constant. On the other hand, errors in transient measurements are dominated by the uncertainty in the fraction of incident light absorbed by the sample and noise in the laser pulse energy. Estimating random errors involved computing the samples' average yield and establishing the standard deviation of the mean.

2.8 Computational Methodology

All density functional theory (DFT) calculations were performed using the projector augmented wave method as implemented in the Vienna Ab initio Simulation Package (VASP). The low temperature experimental crystal structures were used as starting points(e.g., $Pmc21$ for $CH_3NH_3SnBr_3$ and $Pnma$ for $CsSnBr_3$, and the geometries were relaxed using the range-separated hybrid functional HSE06 with the Grimme D3 dispersion correction using Becke-Johnson damping.[52–55] The plane-wave cutoff energy and k-mesh density were converged to a total energy difference of 1 meV/atom for both materials, with a 30% increase in plane-wave cutoff energy during relaxations to avoid Pulay stress effects.

The electrical transport calculations were performed using the AMSET code,[56] which goes beyond the constant relaxation time approximation by calculating several scattering rates explicitly using the momentum relacation time approximation to the Boltzmann transport equation. Scattering from ionized impurities (IMP), acoustic deformation potential (ADP), polar optical phonons (POP), and piezoelectric interactions (PIE) are accounted using common material properties attainable from computational calculations. Density functional perturbation theory (DFPT) calculations using the PBEsol functional were used to calculate the ionic dielectric constants, piezoelectric constants and POP frequency.[57] An "effective phonon frequency" was used where each phonon mode is weighted by the dipole moment it produces, while also neglecting the high frequency intramolecular modes in $MASnBr_3$.[28] Finite difference calculations using the PBEsol functional were used to cal-

culate the elastic constants. Hybrid DFT optical absorption calculations with the inclusion of spin orbit coupling were used to calculate the high-frequency dielectric constants. The input parameters used for AMSET are given in the Supplemental Information (Tables S3, S4, and S5) and a complete account of the mobility calculation methods can be found in Ref. 56.

3 Results

3.1 Structural Characterization

$CH_3NH_3SnBr_3$ and $CsSnBr_3$ form a solid-solution, across a range of compositions of x, including 0, 0.04, 0.1, 0.2, 0.3, 0.8, 0.96, and 1, with a miscibility gap for $0.45 < x < 0.75$ for $(CH_3NH_3)_{1-x}Cs_xSnBr_3$. All single-phase members of the solid solution series crystallize in a cubic perovskite structure (space group: $Pm\bar{3}m$) at room temperature, as illustrated in Figure 1. For samples $0.45 < x < 0.75$, peak splitting in the PXRD indicates two-phase behavior, as shown in Figure S1. As such, those compositions are omitted from further analysis. Rietveld analysis of laboratory PXRD data on samples intimately mixed with a Si powder as an internal standard demonstrates a systematic shift in lattice parameter (Figure S2), consistent with a homogeneous solid solution.

From the crystallographic analysis of temperature-dependent synchrotron X-ray diffraction data, the solid-solution series of $(CH_3NH_3)_{1-x}Cs_xSnBr_3$ exhibits similar T-dependent phase transitions as the end members, as depicted in the phase diagram of Figure 2. On the methylammonium-rich side of the miscibility gap, the compounds transition from cubic $Pm\bar{3}m$ symmetry to orthorhombic $Pmc2_1$ symmetry by way of polar tin off-centering distortions and octahedral rotations below ca. 230 K.[29] However, the triclinic phase appears to be suppressed for $x \geq 0.05$ above $T = 100$ K. The cesium-rich side of the miscibility gap behaves like $CsSnBr_3$, in that octahedral tilting displacements freeze out to yield to $P4/mbm$ symmetry (1 tilt mode, $a^0a^0c^+$) then to $Pnma$ (3 tilt axes, $a^+b^-b^-$). Diffraction data do not

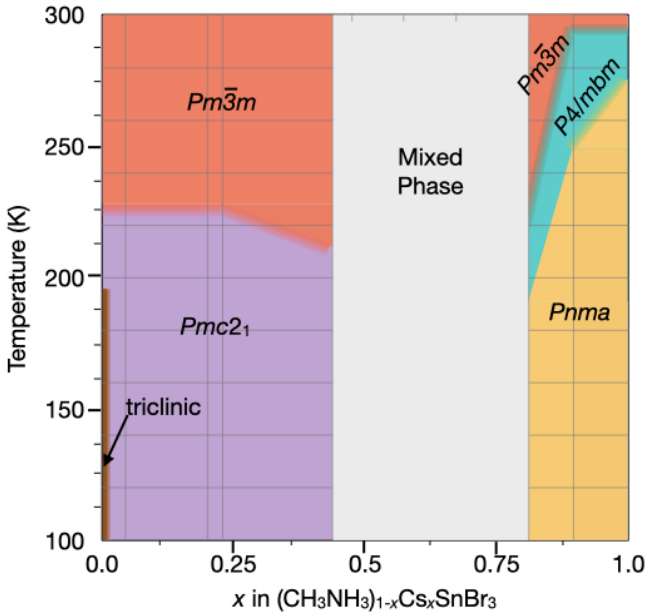

Figure 2: Schematic phase diagram of the solid solution series $(CH_3NH_3)_{1-x}Cs_xSnBr_3$ obtained from analysis of temperature-dependent synchrotron X-ray powder diffraction data. The intersections of the gray grid represent explicitly sampled temperatures and compositions. A two-phase region appears between $0.45 < x < 0.75$.

exhibit evidence for long-range ordering of polar distortions or tin off-centering displacements above 100 K. An extended discussion of the low-temperature diffraction data and symmetry analysis can be found in the Supplemental Information (see Figure S3). This structural phase behavior underpins the analysis of the optical and electronic properties.

3.2 Optical properties

Examination of the optical absorption across the series of compounds, $(CH_3NH_3)_{1-x}Cs_xSnBr_3$, also reveals solid solution behavior with the optical bandgap generally decreasing with x (Figure 3, Table S1). This trend is observed independent of the treatment of the diffuse reflectance spectra; however, the magnitude of the optical bandgap changes with the scaling of the reflectance data used to extract the transition energy (Figure S4 and Figure 3(b)). The overall trend with "x" is anticipated from the nature of bonding and unit cell contraction as the concentration of the smaller cesium ion increases,

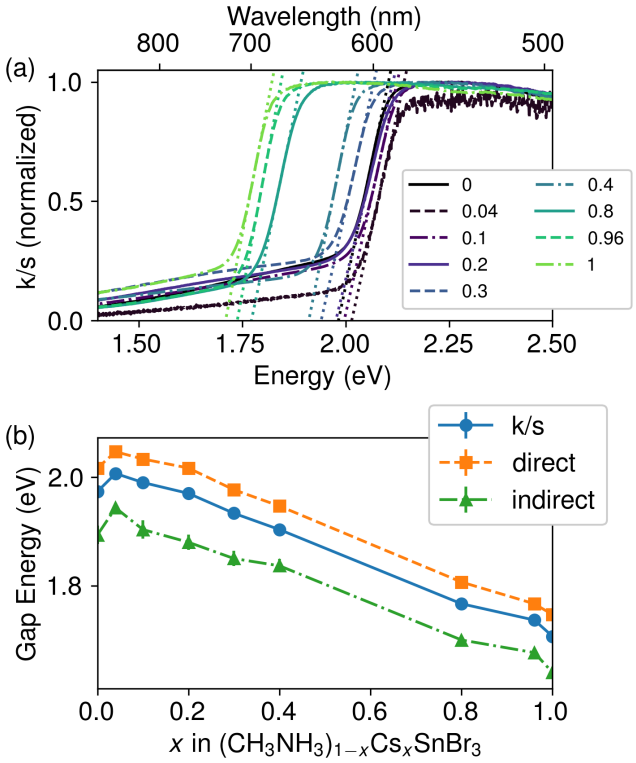

Figure 3: (a) Kubelka-Munk transformation of diffuse reflectance data (k/s) collected from $(CH_3NH_3)_{1-x}Cs_xSnBr_3$ samples. (b) The optical gap extracted from a linear extrapolation of the data in (a) shows a linear decrease in the optical gap energy in with composition, x in $(CH_3NH_3)_{1-x}Cs_xSnBr_3$ (error bars are smaller than the data markers); the magnitude of the gap has a systematic offset depending on how the diffuse reflectance spectra are linearized for parabolic bands with a direct band gap ($(k/s)^2$) or a indirect band gap ($(k/s)^{1/2}$).

as observed from thermal contraction of related phases.[58] The bottom of the conduction band is predominantly composed of anti-bonding states (Sn p,Br p) that increase in energy with increased orbital overlap (e.g., with increasing x); meanwhile, the top of the valence band also has anti-bonding character (Br p, Sn s) that increases in energy to a greater extent with increased orbital overlap.[59] Therefore, the unit cell contraction with increasing x results in a narrowing of the bandgap. The absorbance data for all samples show tailing of absorption below the gap, consistent with the presence of mid-gap electronic states arising from point defects. These defects are likely to arise from adventitious oxidation of tin (II) to tin (IV),[60] which is predicted to be compensated predominantly

by tin vacancies.[61–63] This is discussed further in the context of the microwave conductivity experiments. Together, trends in the phase behavior and optical band gap illustrate solid-solution formation across the series, $(CH_3NH_3)_{1-x}Cs_xSnBr_3$.

3.3 Electronic Properties

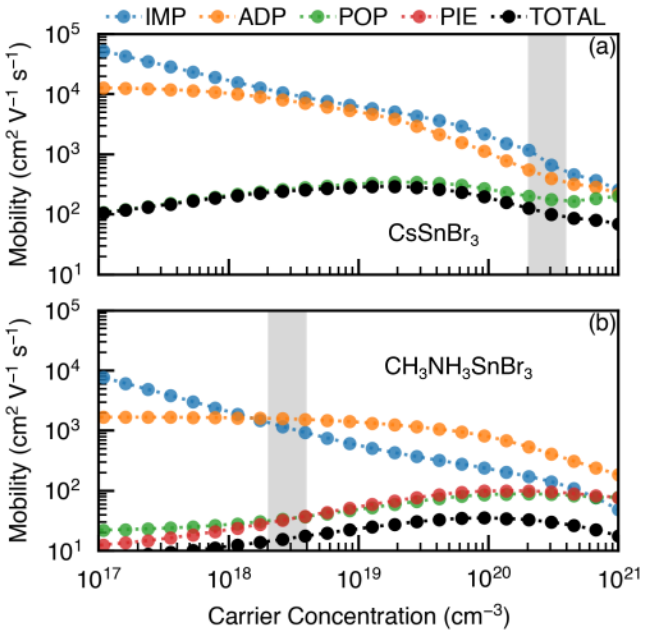

Figure 4: Calculated component and total carrier mobilities as a function of carrier concentration at 300 K for (a) $CsSnBr_3$ and (b) $CH_3NH_3SnBr_3$, using density functional theory. Ionised impurity scattering, IMP (blue); acoustic deformation potential, ADP (orange); polar optical phonon, POP (green); piezoelectric, PIE (red); total mobility (black); and carrier concentrations measured experimentally for these compositions using time-resolved and dark microwave conductivity experiments (grey box).

First principles calculations predict lower carrier mobilities for $CH_3NH_3SnBr_3$ relative to $CsSnBr_3$, but at modest magnitudes attributed to a renormalizatiion of the band structure from distortions. First-principle calculations were used to predict hole mobilities using the ab-initio Scattering and Transport (AMSET) package,[56] with the inclusion of scattering from ionized impurities (IMP), acoustic phonons (ADP), polar optical phonons (POP), and piezoelectric interactions (PIE, for non-centrosymmetric $CH_3NH_3SnBr_3$), with the results

illustrated in Figure 4. We employ the use of the lower-temperature phases ($T = 200$ K), $CH_3NH_3SnBr_3$ ($Pmc2_1$) and $CsSnBr_3$ ($Pnma$), as they likely more accurately reflect the local structure of the material subject to dynamic fluctuations at room temperature, as elaborated in the discussion of the total scattering experiments. Furthermore, these structures are dynamically stable under static DFT calculations using the PBEsol functional (though others find dynamic instabilities using the PBE functional[35]). In both compounds, optical phonon (POP) scattering is the dominant scattering mechanism for the majority of carrier concentrations. Additionally, the non-centrosymmetric crystal structure of $CH_3NH_3SnBr_3$ allows for the piezoelectric effect to contribute to carrier scattering, which combined with a significantly higher conductivity effective mass (0.45 m_e vs 0.11 m_e),[64] results in almost an order of magnitude difference in the predicted hole mobilities. It is important to note that AMSET uses a scattering model and therefore assumes the carrier transport is band-like in nature, an assumption that likely falls apart at high carrier densities.

We conducted a combination of dark and time-resolved microwave conductivity (DMC and TRMC) experiments to evaluate the carrier density, mobility, and dielectric properties as a function of composition. These experiments required decomposition of the real and imaginary parts of the photoconductivity in most cases, and revealed complex trends including the emergence of *negative* components of the real photoconductivity[50] for intermediate compositions ($0 < x < 1$). These results are summarized in Figure S5-S9, including all the microwave resonance curves (Figure S5), the dark conductivity and dielectric constant (Figure S6), conductivity transients (Figure S7), trends in the real and imaginary parts of the transient signal (Figure S8), and the amplitude weighted average lifetime as a function of composition (Figure S9). We provide a physical interpretation of *negative* real "photoconductivity" in the discussion. In the main narrative, we only analyze the positive real component, which was deconvoluted from the total signal by fitting a sum of three exponential components to the transient dynamics and taking average values of the positive real photoconductivity at the lowest commonly measurable fluence among all

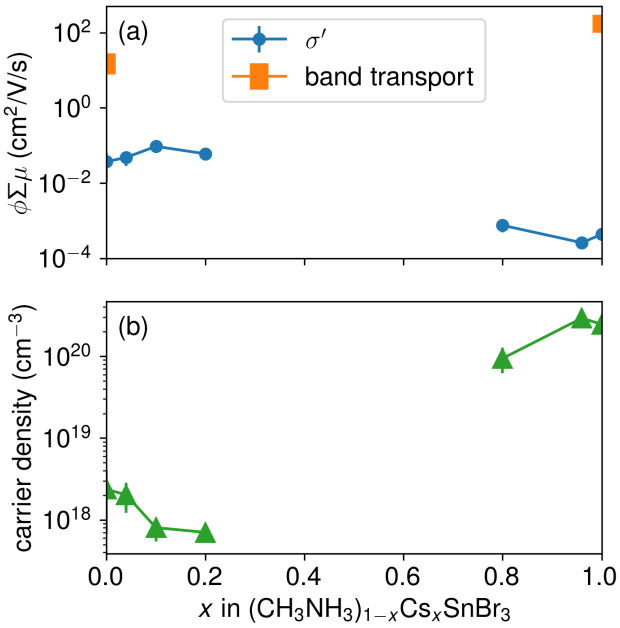

Figure 5: (a) Predicted band transport mobilities from DFT calculations compared to the yield-mobility-product obtained from time-resolved microwave conductivity experiments (σ') (excitation at 532 nm; probe at 9 GHz) as a function of composition x in $(CH_3NH_3)_{1-x}Cs_xSnBr_3$. The trend in mobility opposes those predicted from band transport calculations (Figure 4) (b) Carrier density obtained from analysis of the microwave conductivity experiments as a function of composition x in $(CH_3NH_3)_{1-x}Cs_xSnBr_3$.

the samples.

Combining the positive real photoconductivity with dark conductivity measurements[44] reveals a general trend of increasing carrier concentration and decreasing minimum mobility with increasing Cs incorporation, counter to the trend predicted by theory. As shown in Figure S8, methylammonium-rich samples show visible light fluence-dependent yield-mobility-products in the range of 10^{-2} to 10^{-1} cm^2 V^{-1} s^{-1}; Cs-rich samples show a lower range of values $\approx 10^{-3}$ cm^2 V^{-1} s^{-1} (grey boxes in Figure 4). The dark microwave conductivity measurements[44,46,65] provide the equilibrium conductivity and relative dielectric constant as a function of composition, both of which show a systematic U-shaped trend as a function of composition, where mixed composition samples generally have lower conductivity and relative dielectric constant than the end members, as shown in Figure S6. Combined with the minimum mobility derived from the positive real part of the photocon-

ductivity amplitude (noted in the methods), these data are used to compute the maximum carrier density estimates displayed in Figure 5(b), thus revealing a significantly higher carrier concentration in Cs-rich samples ($> 10^{20}$ cm^{-3}) relative to MA-rich samples ($< 2 \times 10^{18}$ cm^{-3}).

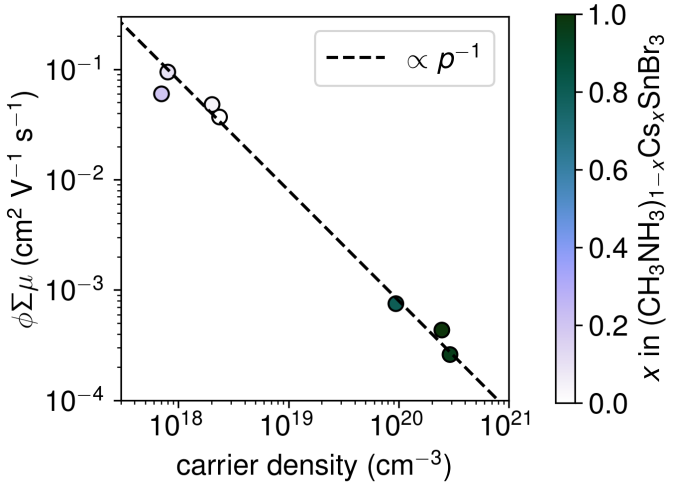

Figure 6: Yield-mobility-product as a function of carrier density (both determined by microwave conductivity) for different compositions x in $(CH_3NH_3)_{1-x}Cs_xSnBr_3$ samples. The short dashed line shows the relation calculated for $\mu \propto p^{-1}$, where mu is the mobility and p is the carrier density.

Examination of the transport behavior extracted from the microwave conductivity experiments reveals a high carrier density that increases with x, with carrier mobility apparently limited by this unintentional doping. Plotting the yield-mobility-product ($\phi\Sigma\mu$) as a function of carrier density (p, Figure 6) reveals a trend of $\mu \propto p^{-1}$, if we assume that $\phi = 1$ for all samples. This linear trend is mirrored in the carrier transport calculations (Figure 4) This strong dependence of the mobility on the inverse of the carrier density is often a sign of significant carrier-carrier scattering and ionized impurity scattering.[66,67] Higher concentrations of ionized impurities and carriers typically enhance ionized impurity scattering[68–70] and intensify electron-electron scattering.[71–73] The systematic trend in carrier

density suggests a link between the materials chemistry and the defect thermochemistry, as elaborated in the discussion.

Analysis of the particle size rules out the alternative explanation that crystallite-size controls the trends in the measured mobility. For small particle sizes, the AC mobility can be limited by the reflection of freely diffusing charge carriers off of crystal boundaries within the microwave probe period (≈ 100 ps).[74–77] The crystal domain sizes found from XRD *are* small enough (150-300 nm) that they could systematically diminish the AC mobility we measure relative to the true intrinsic value, particularly if the latter is high,[76] in the 100's of $cm^2\ V^{-1}\ s^{-1}$ as suggested by theory and single-crystal measurements noted in the introduction. However, our measurements of the particle and crystalline size in this system reveal no systematic trends that could explain the microwave conductivity data, as discussed in the Supporting Information (Figure S14). In the next section we investigate the atomistic structure of these materials using total scattering in an effort to understand why the electronic properties vary in the way we observe.

3.4 Pair Distribution Function Analysis

Pair distribution function analysis of X-ray total scattering reveals the presence of significant dynamic local distortions from the primitive cubic crystal structure. Shown in Figure 7, the PDF analyses for $CsSnBr_3$ and $CH_3NH_3SnBr_3$ show differences from the calculated $Pm\bar{3}m$ structural model, particularly at low interatomic separations ($r < 3.5$ Å), suggesting that the bonding within and between [$SnBr_6$] octahedra is distorted from ideal. These distortions have previously been attributed to dynamic fluctuations of the cubic crystal structure.[10,30] More recent studies on $CH_3NH_3PbBr_3$, $CH_3NH_3PbI_3$, and $CH(NH_2)_2PbBr_3$ revealed that significant diffuse X-ray scattering results from slow dynamic distortions from the cubic crystal structure.[78,79] The dynamic distortions resemble the crystal structure observed after cooling through a phase transition. Inspired by this relationship between dynamic distortions and phonon-driven phase transitions, we employ symmetry-adapted

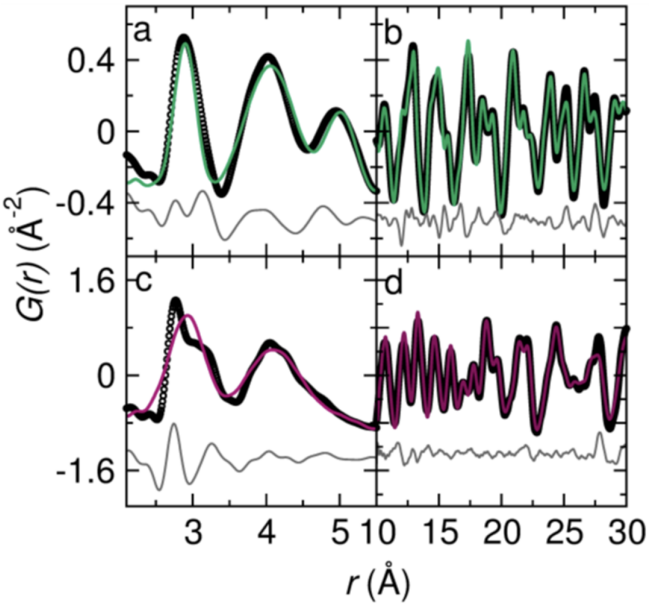

Figure 7: Pair distribution functions obtained from analysis of synchrotron X-ray total scattering data collected at room temperature for (a,b) $CsSnBr_3$ and (c,d) $CH_3NH_3SnBr_3$ (data in black circles), with the r-axis split into two scales (a,c vs b,d) to highlight the Sn–Br bonding environment (a,c). The (a,b) green and (c,d) magenta lines illustrate the pair distribution function calculated from a cubic perovskite structure at room temperature, which cannot capture the local Sn–Br bonding environment.

pair distribution function analysis[40] to understand the nature of the distortions.

Symmetry-adapted pair distribution function analysis reveals a systematic distortion amplitude and character trend across the solid-solution series. Using the $Pmc2_1$ crystal structure of $CH_3NH_3SnBr_3$ as a basis for the symmetry-adapted distortions,[29] it is possible to obtain reasonable fits to the PDF's across the entire range (2-30 Å) for all compositions using only 17 free parameters (overall scale, 3 unit cell constants, 5 mode amplitudes, 2 thermal parameter values, 6 parameters to describe the position and orientation of the MA rigid body) in the model, as illustrated in Figure 8. The composition-dependent mode amplitudes are shown in Figure 9(a). Three distortion modes (Γ_4^- Br A_{2u}, Γ_4^- Br E_u and M_3^+ Br E_u, illustrated in Figure 9(b)) have a significant amplitude across the entire series and offer a comprehensive understanding of the dynamic distortions.

The symmetry-adapted mode analysis of the experimental PDFs reveals a change in

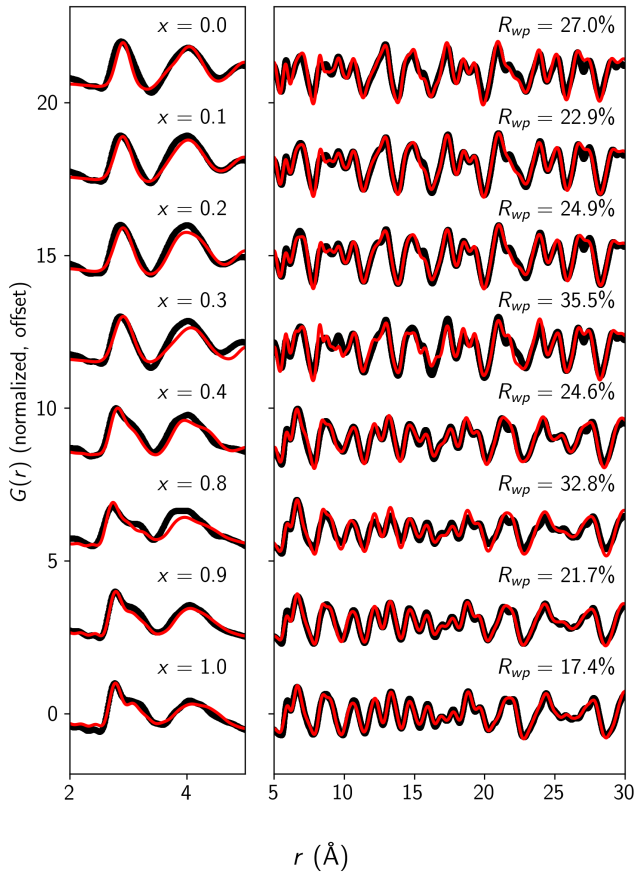

Figure 8: Pair distribution functions obtained from analysis of synchrotron X-ray total scattering data collected at room temperature for solid-solution compounds in the series, $(CH_3NH_3)_{1-x}Cs_xSnBr_3$ (black circles). The red lines are calculated from the refinement of symmetry-adapted displacements of the cubic, $Pm\bar{3}m$ crystal structure down to $Pmc2_1$ symmetry.[29] The structural model fits the data across the entire distance range, r, after including r-dependent peak broadening as described in the Supporting Information. The plot illustrates two different scales of the r-axis (2–5 Å and 5–30 Å) to highlight distortions of the local Sn–Br bonding environment.

Sn–Br–Sn bonding from methylammonium-rich to cesium-rich samples. The M_3^+ Br E_u distortion mode describing in-phase octahedral tilting is present and uniform across the entire series of compounds studied, consistent with the analysis of diffuse X-ray scattering of $A\text{Pb}X_3$.[78,79] The Γ_4^- Cs T_{1u} mode amplitude decreases with increasing x, which either means that the Cs atoms displace as their occupancy decreases or that when the Cs occupancy is low, the PDF is far less sensitive to the actual position of Cs. As x increases, there is a change in the dominant mode of tin off-centering, as exhibited in the behavior of the Γ_4^-

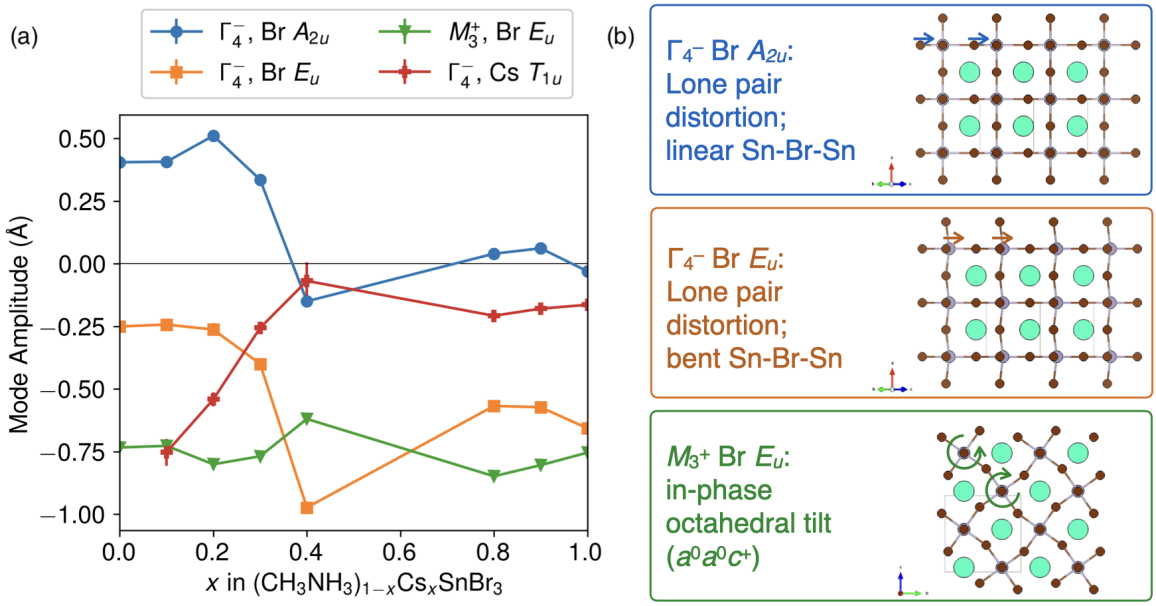

Figure 9: (a) Symmetry-adapted displacement mode amplitudes obtained from refinement against the X-ray PDFs collected at room temperature as a function of composition, x in $(CH_3NH_3)_{1-x}Cs_xSnBr_3$. The M_3^+ mode describing in-phase octahedral tilting (e.g., $a^0a^0c^+$) is constant with x. Within the Γ_4^- family of displacement modes, there is a trade-off of the Γ_4^- A_{2u} mode for the E_u mode with x. The Cs displacement mode amplitude decreases with increasing x for the lowest x values. (b) Illustration of (top) the Γ_4^- Br A_{2u} mode showing the distortion of the [$SnBr_6$] octahedra with retained linear Sn–Br–Sn bond angles, (middle) the Γ_4^- Br E_u mode showing the distortion of the [$SnBr_6$] octahedra with distorted Sn–Br–Sn bond angles (angle $\neq 180°$), and (bottom) the M_3^+ Br E_u in-phase octahedral tilting mode.

Br A_{2u} and Γ_4^- Br E_u modes. At low values of x, the Γ_4^- Br A_{2u} mode amplitude dominates with large, positive values; the sign of the amplitude dictates the direction of the polarization vector. As x increases past 0.3, the mode amplitude of Γ_4^- Br A_{2u} decreases while the magnitude of the mode amplitude of Γ_4^- Br E_u increases. This correlates with a critical difference in the A_{2u} vs E_u mode: the A_{2u} mode preserves a linear Sn–Br–Sn bonding environment between octahedra; the E_u mode yields non-linear Sn–Br–Sn bonding. Such a difference in dynamic distortions has significant potential to influence carrier transport due to the strong dependence of the frontier orbital energies and defect thermodynamics on the bonding geometry.

4 Discussion

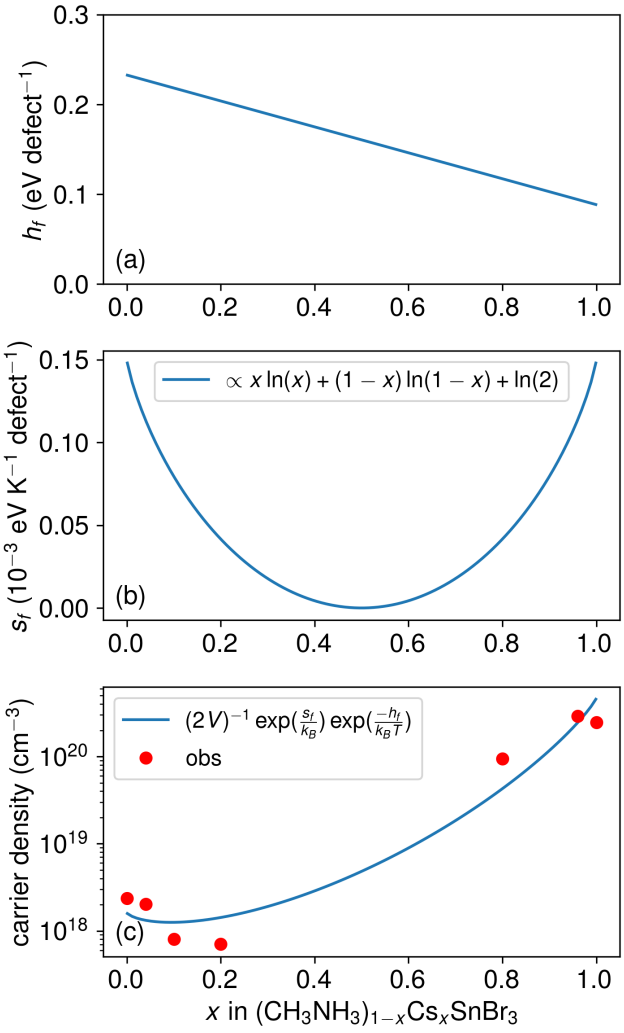

Figure 10: Defect formation thermochemistry for a divalent ionic defect as a function of x in $(CH_3NH_3)_{1-x}Cs_xSnBr_3$: (a) defect formation enthalpy, h_f (eV defect^{-1}), (b) non-configurational defect formation entropy, s_f (eV K^{-1} defect^{-1}), and (c) carrier density, ρ (cm^{-3}), shown with the blue line and the experimental values (observed) in red dots.

The carrier density follows a systematic trend in x that can be modelled by a composition-dependent change in the defect thermochemistry. In general, the Cs-rich samples exhibit a significantly higher carrier density ($\times 10^2$ higher) than MA-rich samples. A previous DFT-based study revealed that doubly-charged tin vacancies (v''_{Sn}) are the lowest energy defect at reasonable chemical potentials for both $(CH_3NH_3)SnBr_3$ and $CsSnBr_3$, and that the de-

fect enthalpy was lowest for $CsSnBr_3$.[80] As such, we assume a linear trend in the average enthalpy of formation per tin vacancy defect in modelling the defect thermochemistry (Figure 10(a)), $h_f = f(x) = h_0 - mx$. This contribution is the dominant factor in describing the non-configurational free energy per defect.

Curiously, the carrier density (Figure 10(c)) decreases with increasing x in the MA-rich samples, and it decreases with decreasing x in the Cs-rich samples. This suggests that alloying somehow inhibits defect formation. We make a simplifying assumption that the formation of a defect in the pristine compounds ($x = 0$ and $x = 1$) is favored by way of the orientational entropy per defect, as described in Ref. 81. We assume that this degeneracy factor is reduced in the alloys, due to reduced local symmetry arising from the disordered A-site cation arrangement, as described in detail in the Supporting Information. While we do not know the exact mathematical form of this degeneracy factor, the expression derived for the configurational entropy of one-site mixing, $s_f = s_0(x\ln(x)+(1-x)\ln(1-x)+\ln(2))$, phenomenologically reproduces this trend (Figure 10(b)).

With expressions for the enthalpy and non-configurational entropy per defect, we model the carrier density as a function of varying A-site to extract the defect thermodynamics. Following the expression:[81]

$$\ln(p) = \ln([c]/2) = \ln(1/2) + \ln(V^{-1}) + s_f/k_B - h_f/(k_B T), \tag{1}$$

where p is the hole carrier density (e.g., the observed values), $[c]$ is the ionic defect concentration (with $[c] = \frac{1}{2}p$ as there are 2 holes for each v''_{Sn}) and V^{-1} is the observed unit cell volume, and using the composition-dependent carrier densities and unit cell volumes (Figure S2(b)), the simplifying descriptions above provide a robust, 3-parameter model (h_0, m, and s_0 in Eqn S7) that describes the observed behavior, as illustrated in Figure 10(c). It is important to recognize that the ionized impurity concentration can be accurately approximated as a constant times the carrier concentration (e.g., $[c] = \frac{1}{2}p$) only when a single type

of dopant is present. An elaborated discussion of the fitted parameters (Table S2), fitted parameters for a monovalent ionic defect (Figure S15), and an alternative Bayesian non-linear regression (Figures S16 and S17) are provided in the Supporting Information. Of note, the assumed defect charge state has little impact on the thermochemical parameters due to the logarithmic relationship.

The local structure obtained from PDF analysis provides insight to the defect thermochemistry. As Cs-rich compounds exhibit further deviations from linear Sn–Br–Sn bonding, this has the potential to disrupt bonding and decrease the tin vacancy enthalpy observed in Figure 10(b) and as previously described.[80] The local structure also resolves compositional trends in the anomalous negative contributions to the photoconductivity observed exclusively in the alloyed samples. This behavior has been reported previously[50] and was attributed primarily to polaron formation involving methylammonium ion orientation. AC conductivity measurements are always "effective" in nature, as the dielectric losses, such as from polar atomic fluctuations, contribute to the effective conductivity. Thus the argument Yamada, et al., make is that trapped electronic charges, which contribute nothing to the real electronic conductivity because of their immobility, make themselves felt by polarizing the surrounding MA cations and decreasing the imaginary part of the permittivity. Our results are consistent with this explanation and build upon it. We only observe significant negative real conductivity for mixed compositions where $0 < x < 1$ in $(CH_3NH_3)_{1-x}Cs_xSnBr_3$. When $x = 0$ there is less carrier trapping in the absence of polar Sn–Br–Sn bond distortions (e.g., Γ_4^- Br E_u), and any orientation or "locking" of MA cations that takes place that could reduce the imaginary permittivity is overwhelmed by the large real conductivity. For $x = 1$, trapping (and carrier density) are maximized, but no MA cations are present to produce the negative imaginary response. Only for the mixed compositions with $0 < x < 1$ do we observe negative transient behavior, which we identify with a photoinduced reduction in both the real and imaginary parts of the permittivity of the sample.

5 Conclusions

In this study we observe a solid-solution between $CH_3NH_3SnBr_3$ and $CsSnBr_3$, with a miscibility gap for $0.45 < x < 0.75$ in $(CH_3NH_3)_{1-x}Cs_xSnBr_3$. All alloyed compounds present as cubic symmetry ($Pm\bar{3}m$) at room temperature. The alloying yields a systematic shift in the optical band gap consistent with the effective compression of the unit cell with increasing cesium content. The alloyed compounds exhibit temperature-dependent phase transitions mirroring that of their proximal pristine phase; although, the transition temperatures are depressed. Synchrotron X-ray total scattering experiments with symmetry-adapted displacement mode analysis of the extracted pair distribution function analysis reveal a change in the distortion modes from more linear Sn–Br–Sn bonding (Γ_4^- Br A_{2u}) to less linear Sn–Br–Sn bonding (Γ_4^- Br E_u) with increasing x. Microwave conductivity experiments across the series of compounds show that Cs substitution reduces carrier mobility, contradicting the expectations of band transport DFT and scattering theory, indicating the influence of Cs on carrier dynamics. The decrease in mobility when comparing $CH_3NH_3SnBr_3$ to $CsSnBr_3$ is accompanied by a systematic increase in both the carrier density and relative dielectric constant of the latter material but with surprising reduction in both properties for intermediate compositions. We use a 3-parameter model to describe the systematic composition dependence of the carrier density to extract the enthalpy and non-configurational entropy per defect. This reveals that the Cs-rich compounds are more prone to systematic oxidation by way of a lower defect enthalpy. The local bonding environment obtained from pair distribution function analysis provides insights to this composition-dependent defect thermochemistry. Additionally, the local bonding environment hints to the origin of the anomalous photoconductivity attributed to trapped charges that polarize surrounding methylammonium, as when $x = 0$ the reduced polar Br–Sn–Br bond distortions or "locking" of MA cations could reduce this factor. While process engineering may be used to ultimately reduce the defect concentrations, the defect-limited mobility and defect thermochemistry in $(CH_3NH_3)_{1-x}Cs_xSnBr_3$ may limit useful applica-

tions in photovoltaic devices, particularly for Cs-rich compositions.

6 Acknowledgements

The work at Colorado State University was supported by grant DE-SC0023316 funded by the U.S. Department of Energy, Office of Science. J.R.N. acknowledges the Leverhulme Trust for granting and A.L. Goodwin for hosting a Visiting Professorship at the Inorganic Chemistry Laboratory, University of Oxford that permitted time for the symmetry-adapted displacement mode analysis and collaboration with U.K. based coauthors. The authors thank the Analytical Resources Core at Colorado State University for instrument access and training (RRID: SCR_021758). The authors thank Dr. Leighanne Gallington for assistance with data collection at the APS, beamline 11-ID-B. Use of the Advanced Photon Source at Argonne National Laboratory was supported by the U. S. Department of Energy, Office of Science, Office of Basic Energy Sciences, under Contract No. DE-AC02-06CH11357. The authors thank D. Olds for assistance with data collection at NSLS-II. This research used Beamline 28-ID-1 (PDF) of the National Synchrotron Light Source II, a U.S. Department of Energy (DOE) Office of Science User Facility operated for the DOE Office of Science by Brookhaven National Laboratory under Contract No. DE-SC0012704. A.N. acknowledges the EPSRC and SFI Centre for Doctoral Training in Advanced Characterisation of Materials (EP/S023259/1) for funding a PhD studentship. This work used the UCL Kathleen, and Myriad HPC Facilities (Kathleen@UCL and Myriad@UCL). Some of the calculations described in this article were performed using the University of Birmingham's BlueBEAR HPC service, the Baskerville Tier 2 HPC service (https://www.baskerville.ac.uk/; funded by the EPSRC and UKRI through the World Class Labs scheme (EP/T022221/1) and the Digital Research Infrastructure programme (EP/W032244/1)), and the Sulis Tier 2 HPC platform hosted by the Scientific Computing Research Technology Platform at the University of Warwick (funded by EPSRC Grant EP/T022108/1 and the HPC Midlands+ con-

sortium). Through our membership of the UK's HEC Materials Chemistry Consortium, which is funded by the UK Engineering and Physical Sciences Research Council (EPSRC; EP/L000202, EP/R029431, EP/T022213), this work also used ARCHER2 UK National Supercomputing Services.

This work was authored in part by the National Renewable Energy Laboratory, operated by Alliance for Sustainable Energy, LLC, for the U.S. Department of Energy (DOE) under Contract No. DE-AC36-08GO28308. Funding for microwave conductivity measurements provided by the Materials Chemistry Program, Materials Sciences and Engineering (MSE) Division, Office of Basic Energy Sciences, U.S. Department of Energy (DE-SC0023316). The views expressed in the article do not necessarily represent the views of the DOE or the U.S. Government. The U.S. Government retains and the publisher, by accepting the article for publication, acknowledges that the U.S. Government retains a nonexclusive, paid-up, irrevocable, worldwide license to publish or reproduce the published form of this work, or allow others to do so, for U.S. Government purposes.

7 Supporting Information

Supporting Information: Additional experimental details pertaining to: composition and temperature-dependent diffraction, alternative analyses of optical properties, microwave resonance experiments and transient analysis, total scattering and pair distribution function analysis, particle and crystal size determination, and alternative defect thermochemical analysis with non-linear Bayesian regression. The text from an exemplary input file for symmetry-adapted displacement mode refinements as implemented in TOPAS v6 is also provided in supplementary file, `MA01Cs09SnBr3.inp.txt`; an interactive notebook for non-linear Bayesian regression is provided in the file, `nonlin-Bayesian.ipynb`.

References

(1) Li, W.; Wang, Z.; Deschler, F.; Gao, S.; Friend, R. H.; Cheetham, A. K. Chemically diverse and multifunctional hybrid organic–inorganic perovskites. *Nature Reviews Materials* **2017**, *2*, 16099.

(2) Jena, A. K.; Kulkarni, A.; Miyasaka, T. Halide Perovskite Photovoltaics: Background, Status, and Future Prospects. *Chemical Reviews* **2019**, *119*, 3036–3103.

(3) Aristidou, N.; Sanchez-Molina, I.; Chotchuangchutchaval, T.; Brown, M.; Martinez, L.; Rath, T.; Haque, S. A. The Role of Oxygen in the Degradation of Methylammonium Lead Trihalide Perovskite Photoactive Layers. *Angewandte Chemie International Edition* **2015**, *54*, 8208–8212.

(4) Aristidou, N.; Eames, C.; Sanchez-Molina, I.; Bu, X.; Kosco, J.; Islam, M. S.; Haque, S. A. Fast oxygen diffusion and iodide defects mediate oxygen-induced degradation of perovskite solar cells. *Nature Communications* **2017**, *8*, 15218.

(5) Leguy, A. M. A.; Hu, Y.; Campoy-Quiles, M.; Alonso, M. I.; Weber, O. J.; Azarhoosh, P.; van Schilfgaarde, M.; Weller, M. T.; Bein, T.; Nelson, J.; Docampo, P.; Barnes, P. R. F. Reversible Hydration of $CH_3NH_3PbI_3$ in Films, Single Crystals, and Solar Cells. *Chemistry of Materials* **2015**, *27*, 3397–3407.

(6) Noel, N. K.; Stranks, S. D.; Abate, A.; Wehrenfennig, C.; Guarnera, S.; Haghighirad, A.-A.; Sadhanala, A.; Eperon, G. E.; Pathak, S. K.; Johnston, M. B.; Petrozza, A.; Herz, L. M.; Snaith, H. J. Lead-free organic–inorganic tin halide perovskites for photovoltaic applications. *Energy Environ. Sci.* **2014**, *7*, 3061–3068.

(7) Rajendra Kumar, G.; Kim, H.-J.; Karupannan, S.; Prabakar, K. Interplay between Iodide and Tin Vacancies in $CsSnI_3$ Perovskite Solar Cells. *The Journal of Physical Chemistry C* **2017**, *121*, 16447–16453.

(8) Hao, F.; Stoumpos, C. C.; Cao, D. H.; Chang, R. P. H.; Kanatzidis, M. G. Lead-free solid-state organic–inorganic halide perovskite solar cells. *Nature Photonics* **2014**, *8*, 489–494.

(9) Marshall, K. P.; Walker, M.; Walton, R. I.; Hatton, R. A. Enhanced stability and efficiency in hole-transport-layer-free $CsSnI_3$ perovskite photovoltaics. *Nature Energy* **2016**, *1*, 16178.

(10) Laurita, G.; Fabini, D. H.; Stoumpos, C. C.; Kanatzidis, M. G.; Seshadri, R. Chemical tuning of dynamic cation off-centering in the cubic phases of hybrid tin and lead halide perovskites. *Chemical Science* **2017**, *8*, 5628–5635.

(11) Stoumpos, C. C.; Frazer, L.; Clark, D. J.; Kim, Y. S.; Rhim, S. H.; Freeman, A. J.; Ketterson, J. B.; Jang, J. I.; Kanatzidis, M. G. Hybrid Germanium Iodide Perovskite Semiconductors: Active Lone Pairs, Structural Distortions, Direct and Indirect Energy Gaps, and Strong Nonlinear Optical Properties. *Journal of the American Chemical Society* **2015**, *137*, 6804–6819.

(12) Worhatch, R. J.; Kim, H.; Swainson, I. P.; Yonkeu, A. L.; Billinge, S. J. L. Study of Local Structure in Selected Organic–Inorganic Perovskites in the $Pm\bar{3}m$ Phase. *Chemistry of Materials* **2008**, *20*, 1272–1277.

(13) Fabini, D. H.; Seshadri, R.; Kanatzidis, M. G. The underappreciated lone pair in halide perovskites underpins their unusual properties. *MRS Bulletin* **2020**, *45*, 467–477.

(14) Jung, M.-C.; Raga, S. R.; Qi, Y. Properties and solar cell applications of Pb-free perovskite films formed by vapor deposition. *RSC Advances* **2016**, *6*, 2819–2825.

(15) López, C. A.; Abia, C.; Gainza, J.; Kayser, P.; Nemes, N. N.; Dura, O. J.; Martínez, J. L.; Fernández-Díaz, M. T.; Álvarez Galván, C.; Alonso, J. A. Structural evolution, optical gap and thermoelectric properties of $CH_3NH_3SnBr_3$ hybrid perovskite, prepared by mechanochemistry. *Materials Advances* **2021**, *2*, 3620–3628.

(16) Chiarella, F.; Zappettini, A.; Licci, F.; Borriello, I.; Cantele, G.; Ninno, D.; Cassinese, A.; Vaglio, R. Combined experimental and theoretical investigation of optical, structural, and electronic properties of $CH_3NH_3SnX_3$ thin films (X = Cl, Br). *Physical Review B—Condensed Matter and Materials Physics* **2008**, *77*, 045129.

(17) Song, T.-B.; Yokoyama, T.; Stoumpos, C. C.; Logsdon, J.; Cao, D. H.; Wasielewski, M. R.; Aramaki, S.; Kanatzidis, M. G. Importance of Reducing Vapor Atmosphere in the Fabrication of Tin-Based Perovskite Solar Cells. *Journal of the American Chemical Society* **2017**, *139*, 836–842.

(18) Peedikakkandy, L.; Bhargava, P. Composition dependent optical, structural and photoluminescence characteristics of cesium tin halide perovskites. *RSC Advances* **2016**, *6*, 19857–19860.

(19) Sabba, D.; Mulmudi, H. K.; Prabhakar, R. R.; Krishnamoorthy, T.; Baikie, T.; Boix, P. P.; Mhaisalkar, S.; Mathews, N. Impact of Anionic Br– Substitution on Open Circuit Voltage in Lead Free Perovskite ($CsSnI_{3-x}Br_x$) Solar Cells. *The Journal of Physical Chemistry C* **2015**, *119*, 1763–1767.

(20) Cao, L.; Gu, S.-M.; Liu, B.; Huang, L.; Zhang, J.; Zhu, Y.; Wang, J. Highly Ambient Stable $CsSnBr_3$ Perovskite via a New Facile Room-Temperature "Coprecipitation" Strategy. *ACS Applied Materials & Interfaces* **2023**, *15*, 30409–30416.

(21) Gupta, S.; Bendikov, T.; Hodes, G.; Cahen, D. $CsSnBr_3$, A Lead-Free Halide Perovskite for Long-Term Solar Cell Application: Insights on SnF_2 Addition. *ACS Energy Letters* **2016**, *1*, 1028–1033.

(22) Moghe, D.; Wang, L.; Traverse, C. J.; Redoute, A.; Sponseller, M.; Brown, P. R.; Bulović, V.; Lunt, R. R. All vapor-deposited lead-free doped $CsSnBr_3$ planar solar cells. *Nano Energy* **2016**, *28*, 469–474.

(23) Eperon, G. E.; Hörantner, M. T.; Snaith, H. J. Metal halide perovskite tandem and multiple-junction photovoltaics. *Nature Reviews Chemistry* **2017**, *1*, 0095.

(24) Chiarella, F.; Ferro, P.; Licci, F.; Barra, M.; Biasiucci, M.; Cassinese, A.; Vaglio, R. Preparation and transport properties of hybrid organic–inorganic $CH_3NH_3SnBr_3$ films. *Applied Physics A* **2006**, *86*, 89–93.

(25) Wu, Y.; Zhou, H.; Yin, J.; Zhang, X. Growth, structural, optical and electronic transport properties of tetragonal $CH_3NH_3SnBr_3$ perovskite single crystals. *Dalton Transactions* **2022**, *51*, 4623–4626.

(26) Jia, J.; Wang, R.; Mu, H. Exciton dynamics and photoresponse behavior of the in situ annealed $CsSnBr_3$ perovskite films synthesized by thermal evaporation. *Nanotechnology* **2022**, *33*, 345503.

(27) Ying, Y.; Luo, X.; Huang, H. Pressure-Induced Topological Nontrivial Phase and Tunable Optical Properties in All-Inorganic Halide Perovskites. *The Journal of Physical Chemistry C* **2018**, *122*, 17718–17725.

(28) Frost, J. M. Calculating Polaron Mobility in Halide Perovskites. *Physical Review B* **2017**, *96*, 195202.

(29) Swainson, I.; Chi, L.; Her, J.-H.; Cranswick, L.; Stephens, P.; Winkler, B.; Wilson, D. J.; Milman, V. Orientational ordering, tilting and lone-pair activity in the perovskite methylammonium tin bromide, $CH_3NH_3SnBr_3$. *Acta Crystallographica Section B Structural Science* **2010**, *66*, 422–429.

(30) Fabini, D. H.; Laurita, G.; Bechtel, J. S.; Stoumpos, C. C.; Evans, H. A.; Kontos, A. G.; Raptis, Y. S.; Falaras, P.; Van der Ven, A.; Kanatzidis, M. G.; Seshadri, R. Dynamic Stereochemical Activity of the Sn^{2+} Lone Pair in Perovskite $CsSnBr_3$. *Journal of the American Chemical Society* **2016**, *138*, 11820–11832.

(31) Chung, I. J.; Song, J. H.; Im, J.; Androulakis, J. G.; Malliakas, C. D.; Li, H.; Freeman, A. J.; Kenney, J. T.; Kanatzidis, M. G. $CsSnI_3$: Semiconductor or metal? High electrical conductivity and strong near-infrared photoluminescence from a single material. High hole mobility and phase-transitions. *Journal of the American Chemical Society* **2012**, *134 20*, 8579–87.

(32) Yamada, K.; Funabiki, S.; Horimoto, H.; Matsui, T.; Okuda, T.; Ichiba, S. Structural phase transitions of the polymorphs of $CsSnI_3$ by means of rietveld analysis of the X-ray diffraction. *Chemistry Letters* **1991**, *20*, 801–804.

(33) Fujii, Y.; Hoshino, S.; Yamada, Y.; Shirane, G. Neutron-scattering study on phase transitions of $CsPbCl_3$. *Physical Review B* **1974**, *9*, 4549–4559.

(34) Hirotsu, S.; Harada, J.; Iizumi, M.; Gesi, K. Structural Phase Transitions in $CsPbBr_3$. *Journal of the Physical Society of Japan* **1974**, *37*, 1393–1398.

(35) Fabini, D. H.; Honasoge, K.; Cohen, A.; Bette, S.; McCall, K. M.; Stoumpos, C. C.; Klenner, S.; Zipkat, M.; Hoang, L. P.; Nuss, J.; Kremer, R. K.; Kanatzidis, M. G.; Yaffe, O.; Kaiser, S.; Lotsch, B. V. Noncollinear Electric Dipoles in a Polar Chiral Phase of $CsSnBr_3$ Perovskite. *Journal of the American Chemical Society* **2024**, *146*, 15701–15717.

(36) Onoda-Yamamuro, N.; Matsuo, T.; Suga, H. Thermal, electric, and dielectric properties of $CH_3NH_3SnBr_3$ at low temperatures. *The Journal of Chemical Thermodynamics* **1991**, *23*, 987–999.

(37) Juhás, P.; Davis, T.; Farrow, C.; Billinge, S. PDFgetX3: a rapid and highly automatable program for processing powder diffraction data into total scattering pair distribution functions. *Journal of Applied Crystallography* **2013**, *46*, 560–566.

(38) Farrow, C. L.; Juhas, P.; Liu, J. W.; Bryndin, D.; Božin, E. S.; Bloch, J.; Proffen, T.;

Billinge, S. J. L. PDFfit2 and PDFgui: computer programs for studying nanostructure in crystals. *Journal of Physics: Condensed Matter* **2007**, *19*, 335219.

(39) Campbell, B. J.; Stokes, H. T.; Tanner, D. E.; Hatch, D. M. ISODISPLACE: a web-based tool for exploring structural distortions. *Journal of Applied Crystallography* **2006**, *39*, 607–614.

(40) Bird, T. A.; Herlihy, A.; Senn, M. S. Symmetry-adapted pair distribution function analysis (SAPA): a novel approach to evaluating lattice dynamics and local distortions from total scattering data. *Journal of Applied Crystallography* **2021**, *54*, 1514–1520.

(41) Sangiorgio, B.; Bozin, E. S.; Malliakas, C. D.; Fechner, M.; Simonov, A.; Kanatzidis, M. G.; Billinge, S. J. L.; Spaldin, N. A.; Weber, T. Correlated local dipoles in PbTe. *Physical Review Materials* **2018**, *2*, 085402.

(42) Jeong, I.-K.; Heffner, R. H.; Graf, M. J.; Billinge, S. J. L. Lattice dynamics and correlated atomic motion from the atomic pair distribution function. *Physical Review B* **2003**, *67*, 104301.

(43) Rasband, W. S. ImageJ. Bethesda, Maryland, USA: US National Institutes of Health. 1997.

(44) Reid, O. G.; Moore, D. T.; Li, Z.; Zhao, D.; Yan, Y.; Zhu, K.; Rumbles, G. Quantitative analysis of time-resolved microwave conductivity data. *Journal of Physics D: Applied Physics* **2017**, *50*, 493002.

(45) Savenije, T. J.; Ferguson, A. J.; Kopidakis, N.; Rumbles, G. Revealing the Dynamics of Charge Carriers in Polymer:Fullerene Blends Using Photoinduced Time-Resolved Microwave Conductivity. *The Journal of Physical Chemistry C* **2013**, *117*, 24085–24103.

(46) Earley, J. D.; Zieleniewska, A.; Ripberger, H. H.; Shin, N. Y.; Lazorski, M. S.; Mast, Z. J.; Sayre, H. J.; McCusker, J. K.; Scholes, G. D.; Knowles, R. R.; Reid, O. G.;

Rumbles, G. Ion-pair reorganization regulates reactivity in photoredox catalysts. *Nature Chemistry* **2022**, *14*, 746–753.

(47) Yuan, Z. et al. Discovery of the Zintl-phosphide $BaCd_2P_2$ as a long carrier lifetime and stable solar absorber. *Joule* **2024**, *8*, 1412–1429.

(48) Schins, J. M.; Talgorn, E. Conductive response of a photo-excited sample in a radio-frequent driven resonance cavity. *Review of Scientific Instruments* **2011**, *82*, 064703.

(49) Saeki, A.; Yasutani, Y.; Oga, H.; Seki, S. Frequency-Modulated Gigahertz Complex Conductivity of TiO_2 Nanoparticles: Interplay of Free and Shallowly Trapped Electrons. *The Journal of Physical Chemistry C* **2014**, *118*, 22561–22572.

(50) Yamada, K.; Nishikubo, R.; Oga, H.; Ogomi, Y.; Hayase, S.; Kanno, S.; Imamura, Y.; Hada, M.; Saeki, A. Anomalous Dielectric Behavior of a Pb/Sn Perovskite: Effect of Trapped Charges on Complex Photoconductivity. *ACS Photonics* **2018**, *5*, 3189–3197.

(51) Yamada, K.; Suzuki, H.; Abe, R.; Saeki, A. Complex Photoconductivity Reveals How the Nonstoichiometric Sr/Ti Affects the Charge Dynamics of a $SrTiO_3$ Photocatalyst. *The Journal of Physical Chemistry Letters* **2019**, *10*, 1986–1991.

(52) Heyd, J.; Scuseria, G. E.; Ernzerhof, M. Hybrid Functionals Based on a Screened Coulomb Potential. *J. Chem. Phys.* **2003**, *118*, 8207–8215.

(53) Krukau, A. V.; Vydrov, O. A.; Izmaylov, A. F.; Scuseria, G. E. Influence of the Exchange Screening Parameter on the Performance of Screened Hybrid Functionals. *J. Chem. Phys.* **2006**, *125*, 224106.

(54) Grimme, S.; Antony, J.; Ehrlich, S.; Krieg, H. A Consistent and Accurate Ab Initio Parametrization of Density Functional Dispersion Correction (DFT-D) for the 94 Elements H-Pu. *The Journal of Chemical Physics* **2010**, *132*, 154104.

(55) Grimme, S.; Ehrlich, S.; Goerigk, L. Effect of the Damping Function in Dispersion Corrected Density Functional Theory. *Journal of Computational Chemistry* **2011**, *32*, 1456–1465.

(56) Ganose, A. M.; Park, J.; Faghaninia, A.; Woods-Robinson, R.; Persson, K. A.; Jain, A. Efficient Calculation of Carrier Scattering Rates from First Principles. *Nature Communications* **2021**, *12*, 2222.

(57) Perdew, J. P.; Ruzsinszky, A.; Csonka, G. I.; Vydrov, O. A.; Scuseria, G. E.; Constantin, L. A.; Zhou, X.; Burke, K. Restoring the Density-Gradient Expansion for Exchange in Solids and Surfaces. *Physical Review Letters* **2008**, *100*, 136406.

(58) Mozur, E. M.; Trowbridge, J. C.; Maughan, A. E.; Gorman, M. J.; Brown, C. M.; Prisk, T. R.; Neilson, J. R. Dynamical Phase Transitions and Cation Orientation-Dependent Photoconductivity in $CH(NH_2)_2PbBr_3$. *ACS Materials Letters* **2019**, *1*, 260–264.

(59) Tao, S.; Schmidt, I.; Brocks, G.; Jiang, J.; Tranca, I.; Meerholz, K.; Olthof, S. Absolute energy level positions in tin- and lead-based halide perovskites. *Nature Communications* **2019**, *10*, 2560.

(60) Gu, S.; Lin, R.; Han, Q.; Gao, Y.; Tan, H.; Zhu, J. Tin and Mixed Lead–Tin Halide Perovskite Solar Cells: Progress and their Application in Tandem Solar Cells. *Advanced Materials* **2020**, *32*, 1907392.

(61) Ricciarelli, D.; Meggiolaro, D.; Ambrosio, F.; De Angelis, F. Instability of Tin Iodide Perovskites: Bulk p-Doping versus Surface Tin Oxidation. *ACS Energy Letters* **2020**, *5*, 2787–2795.

(62) Meggiolaro, D.; Ricciarelli, D.; Alasmari, A. A.; Alasmary, F. A. S.; De Angelis, F. Tin versus Lead Redox Chemistry Modulates Charge Trapping and Self-Doping in

Tin/Lead Iodide Perovskites. *The Journal of Physical Chemistry Letters* **2020**, *11*, 3546–3556.

(63) Shi, T.; Zhang, H.-S.; Meng, W.; Teng, Q.; Liu, M.; Yang, X.; Yan, Y.; Yip, H.-L.; Zhao, Y.-J. Effects of organic cations on the defect physics of tin halide perovskites. *Journal of Materials Chemistry A* **2017**, *5*, 15124–15129.

(64) Gibbs, Z. M.; Ricci, F.; Li, G.; Zhu, H.; Persson, K.; Ceder, G.; Hautier, G.; Jain, A.; Snyder, G. J. Effective Mass and Fermi Surface Complexity Factor from Ab Initio Band Structure Calculations. *npj Computational Materials* **2017**, *3*, 1–7.

(65) Ferguson, A. J.; Reid, O. G.; Nanayakkara, S. U.; Ihly, R.; Blackburn, J. L. Efficiency of Charge-Transfer Doping in Organic Semiconductors Probed with Quantitative Microwave and Direct-Current Conductance. **2018**, *9*, 6864–6870.

(66) Ortiz, B. R.; Crawford, C. M.; McKinney, R. W.; Parilla, P. A.; Toberer, E. S. Thermoelectric properties of bromine filled $CoSb_3$ skutterudite. *Journal of Materials Chemistry A* **2016**, *4*, 8444–8450.

(67) Shuai, J.; Mao, J.; Song, S.; Zhu, Q.; Sun, J.; Wang, Y.; He, R.; Zhou, J.; Chen, G.; Singh, D. J.; Ren, Z. Tuning the carrier scattering mechanism to effectively improve the thermoelectric properties. *Energy & Environmental Science* **2017**, *10*, 799–807.

(68) Long, D.; Myers, J. Ionized-Impurity Scattering Mobility of Electrons in Silicon. *Physical Review* **1959**, *115*, 1107–1118.

(69) Chattopadhyay, D.; Queisser, H. J. Electron scattering by ionized impurities in semiconductors. *Reviews of Modern Physics* **1981**, *53*, 745–768.

(70) Brooks, H. *Advances in Electronics and Electron Physics*; Elsevier, 1955; p 85–182.

(71) Debye, P. P.; Conwell, E. M. Electrical Properties of N-Type Germanium. *Phys. Rev.* **1954**, *93*, 693–706.

(72) Hartman, R. Temperature Dependence of the Low-Field Galvanomagnetic Coefficients of Bismuth. *Physical Review* **1969**, *181*, 1070–1086.

(73) Thompson, A. H. Electron-Electron Scattering in TiS_2. *Phys. Rev. Lett.* **1975**, *35*, 1786–1789.

(74) Prins, P.; Grozema, F. C.; Schins, J. M.; Siebbeles, L. D. A. Frequency dependent mobility of charge carriers along polymer chains with finite length. *physica status solidi (b)* **2006**, *243*, 382–386.

(75) Bird, M. J.; Reid, O. G.; Cook, A. R.; Asaoka, S.; Shibano, Y.; Imahori, H.; Rumbles, G.; Miller, J. R. Mobility of Holes in Oligo- and Polyfluorenes of Defined Lengths. *The Journal of Physical Chemistry C* **2014**, *118*, 6100–6109.

(76) Reid, O. G.; Yang, M.; Kopidakis, N.; Zhu, K.; Rumbles, G. Grain-Size-Limited Mobility in Methylammonium Lead Iodide Perovskite Thin Films. *ACS Energy Letters* **2016**, *1*, 561–565.

(77) Cocker, T. L.; Baillie, D.; Buruma, M.; Titova, L. V.; Sydora, R. D.; Marsiglio, F.; Hegmann, F. A. Microscopic origin of the Drude-Smith model. *Physical Review B* **2017**, *96*, 205439.

(78) Weadock, N. J. et al. The nature of dynamic local order in $CH_3NH_3PbI_3$ and $CH_3NH_3PbBr_3$. *Joule* **2023**, *7*, 1051–1066.

(79) Dubajic, M. et al. Dynamic Nanodomains Dictate Macroscopic Properties in Lead Halide Perovskites. *arXiv* **2024**, 2404.14598.

(80) Kim, E. H.; Lee, J. H.; Kim, S. H.; Gu, J. H.; Lee, D. A-Site Effect on the Oxidation Process of Sn-Halide Perovskite: First-Principles Calculations. *The Journal of Physical Chemistry Letters* **2021**, *12*, 9691–9696.

(81) Mosquera-Lois, I.; Kavanagh, S. R.; Klarbring, J.; Tolborg, K.; Walsh, A. Imperfections are not 0 K: free energy of point defects in crystals. *Chemical Society Reviews* **2023**, *52*, 5812–5826.

TOC Graphic

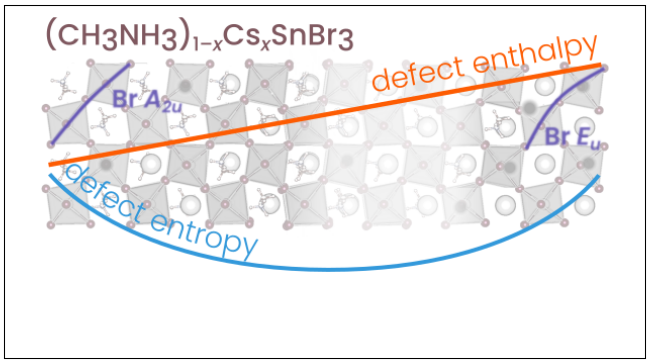
(CH3NH3)1−xCsxSnBr3
defect enthalpy
Br A2u
Br Eu
defect entropy